A dynamic high-resolution simulation of 2-D elastic-plastic crack problems

G. Giese, M. Fey

Abstract In this paper we present a numerical method for performing higher-order simulations of elastic-plastic waves in solids and we illustrate the accuracy of our approach by various numerical simulations of wave phenomena around cracks. The simulation of crack problems in solids is especially challenging, since the singularities in physical variables occurring at the crack are particularly difficult for numerical schemes to simulate, but they create many interesting physical effects.

1
Introduction

There is a huge variety of numerical schemes for solving hyperbolic partial differential equations (cf [1, 7, 8, 20]), including special schemes for the elastic plastic wave equation in solids (cf [9–14]). Most of them are finite volume schemes, which update cell averages in every time-step by calculating fluxes over the cell-borders. In [2] and [3] Fey presented a scheme called Method of Transport for calculating these fluxes in high order in space and time for hyperbolic conservation laws in fluid mechanics in several space dimensions, which we extended to the elastic-plastic wave equation in [4] and [5], which is not a pure conservation law anymore. The main advantage of the method presented in [4] and [5] is that (in principle) it can be implemented in any order for the approximation in both space and time.

The purpose of this paper is to apply our numerical methodology to a challenging class of physical problems, i.e. crack problems in solids. Cracks are particularly difficult to simulate since they typically produce singularities in stress components, especially at the crack-tip. Further, many numerical methods of low order (e.g. first or second order schemes) have to perform a refinement of the numerical grid around the crack-tip to obtain good numerical results, which is costly implementation-wise and computation-wise. We will show that our method yields an excellent resolution of wave phenomena around cracks even when using a Cartesian grid due to the use of

G. Giese (✉), M. Fey
Seminar for Applied Mathematics,
Swiss Federal Institute of Technology, Zurich,
Switzerland.
e-mail: ggiese@Kpmg.comx

higher order approximations. Nevertheless, it is important to mention that even when using a high-order method, in certain situations the usage of an adapted grid around the crack-tip is advantageous, e.g. for calculating transient dynamic stress intensity factors.

Our paper briefly explains the model equations under consideration and the Method of Transport for solving the elastic-plastic wave equation. Then, we simulate several interesting crack problems, discussing the physical behavior or elastic-plastic waves around a crack.

2
The elastic-plastic wave equation

We use a formulation of the elastic-plastic wave equation, which is based on the assumption of small strains, i.e. it is a linearization of the general flow equations (cf. [6, 15]). Furthermore, we use a formulation of the elastic-plastic wave equation as a first order system, which means we have to use three physical variables: The symmetric stress tensor $\underline{\sigma}$, the symmetric strain tensor $\underline{\epsilon}$ and the velocity vector $\vec{v}$. Furthermore, we need the deviatoric stress tensor $\underline{s}$ which is defined as $s_{ij} = \sigma_{ij} - \frac{1}{3}\delta_{ij}\sigma_{kk}$. The system consists of equations describing the conservation of momentum, the compatibility relations between velocity and strain variables and the Prandtl model equations for describing the relationship between stress and strain (cf [18]):

Conservation of momentum:

$$\frac{\partial}{\partial t}v_i = \frac{1}{\rho}\sum_{j=1}^{3}\frac{\partial}{\partial x_j}\sigma_{ij}(\rho = \text{density}) \qquad (1)$$

Compatibility relationship:

$$\frac{\partial}{\partial t}\epsilon_{ij} = \frac{1}{2}\left(\frac{\partial}{\partial x_j}v_i + \frac{\partial}{\partial x_i}v_j\right) \quad i \leq j = 1,\ldots,3 \qquad (2)$$

Stress-strain relationship:

$$\frac{\partial}{\partial t}\epsilon_{ij} = \frac{1+v}{E}\frac{\partial}{\partial t}\sigma_{ij} - \frac{v}{E}\delta_{ij}\frac{d}{dt}\sigma_{kk} + s_{ij}\frac{d}{dt}\chi \qquad (3)$$

with v = Poisson's ratio, E = Young's modulus and the function $\frac{d}{dt}\chi$ detailed below describing the plastic flow. For elasticity equation (3) reduces with $\frac{d}{dt}\chi \equiv 0$ to Hooke's law. In order to distinguish between elastic and plastic deformation we use the so-called von Mises yield function (cf [17]):

$$f(\underline{s}) = \frac{1}{2}s_{ij}s_{ij} =: \kappa^2. \qquad (4)$$
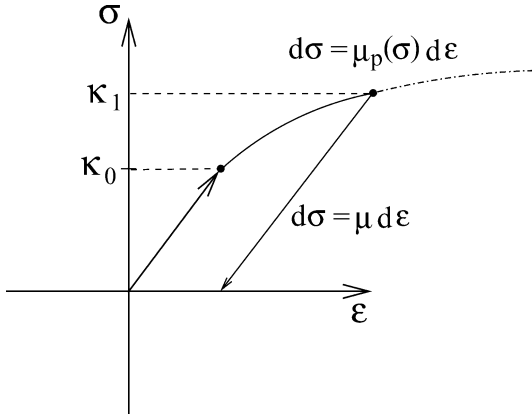
Fig. 1. Response of the strain variable ϵ to the stress σ in the case when hysteresis occurs

Basically, plasticity occurs in a certain point if the current function $\kappa(t)$ in that point attains the value of $\kappa_0(t)$, which is the maximal value of $\kappa(t)$ in the past, i.e. with

$$\kappa_0(t) = \max_{t_0 \le t' \le t} \kappa(t')$$

three different cases may occur:

$\kappa(t) < \kappa_0(t)$: Elastic deformation.
$\kappa(t) = \kappa_0(t)$ and $\frac{d}{dt}\kappa \le 0$: Elastic deformation.
$\kappa(t) = \kappa_0(t)$ and $\frac{d}{dt}\kappa > 0$: Plastic deformation.

This plasticity model reduces to the well-known hysteresis-curve as shown in Fig. 1 in the case of one stress and one strain variable.

In Fig. 1, for small stresses, i.e. $|\sigma| \le \kappa_0$ the relationship is linear (Hooke's law). However, if the stress $|\sigma|$ exceeds a certain value κ_0 then plastic flow occurs. Furthermore, unloading processes are always assumed to be elastic in our plasticity model. After the plastic loading and the elastic unloading process, plasticity will occur again if $|\sigma| \ge \kappa_1$ with κ_1 being the largest value of the stress $|\sigma|$ in the past.

Furthermore, for this yield-criterion the function $\frac{d}{dt}\chi$ from Eq. (3) can be written in the form

$$\frac{d}{dt}\chi = \frac{1}{2\kappa}\left(\frac{1}{\mu_p(\kappa)} - \frac{1}{\mu}\right)\frac{d}{dt}\kappa \tag{5}$$

with a measured function $\mu_p(\kappa) \le \mu$ (cf. Fig. 1) and the elastic shear modulus $\mu = \frac{E}{2(1+\nu)}$. Hence, we have a system of the form[1]

$$V_t + \nabla \cdot c\underline{L}(U) = 0$$
$$(c = \text{wave-speed, will be specified later}) \tag{6}$$

$$\underline{\sigma}_t = \underline{\mathcal{C}}(\underline{\sigma}) : \underline{\epsilon}_t \tag{7}$$

where we defined the vectors

$$V = (v_1, v_2, v_3, \epsilon_{11}, \epsilon_{22}, \epsilon_{33}, \epsilon_{12}, \epsilon_{13}, \epsilon_{23})^T \tag{8}$$

$$U = (v_1, v_2, v_3, \sigma_{11}, \sigma_{22}, \sigma_{33}, \sigma_{12}, \sigma_{13}, \sigma_{23})^T. \tag{9}$$

Equation (6) summarizes the conservation of momentum (1) and the compatibility relations (2) ($\underline{L}(U)$ is a linear function of U, since both equations are linear) and Eq. (7) contains the stress-strain relationship from (3) with the rank-4 tensor $\underline{\mathcal{C}}(\underline{\sigma})$.

It is noteworthy that the system (6), (7) is not (cannot be written as) a pure hyperbolic conservation law, unless the material is purely elastic where the matrix $\underline{\mathcal{C}}$ is constant.

2.1
Model equation in 2-D
Without loss of generality we demonstrate our approach for a solid under the so-called plane strain condition (cf [15]), i.e. the z-component of the displacement and velocity vector is vanishing:

$$\epsilon_{13} = \epsilon_{23} = \epsilon_{33} = \sigma_{23} = \sigma_{13} = v_3 \equiv 0. \tag{10}$$

Hence, the flux Eq. (6) reduces to:

$$\begin{pmatrix} v_1 \\ v_2 \\ \epsilon_{11} \\ \epsilon_{22} \\ \epsilon_{33} \\ \epsilon_{12} \end{pmatrix}_t = \begin{pmatrix} \frac{\sigma_{11}}{\rho} \\ \frac{\sigma_{12}}{\rho} \\ v_1 \\ 0 \\ 0 \\ \frac{1}{2}v_2 \end{pmatrix}_x + \begin{pmatrix} \frac{\sigma_{12}}{\rho} \\ \frac{\sigma_{22}}{\rho} \\ 0 \\ v_2 \\ 0 \\ \frac{1}{2}v_1 \end{pmatrix}_y \tag{11}$$

Although ϵ_{33} is constant according to Eqs. (10) and (11), we leave ϵ_{33} in the equation for the following ideas, because when investigating elastic-plastic waves we will replace strains with stresses and the corresponding stress component σ_{33} does not vanish.

The general stress-strain relationship contained in Eqs. (3) and (5) reduces under the assumption (10) to

$$\begin{pmatrix} \dot{\epsilon}_{11} \\ \dot{\epsilon}_{22} \\ \dot{\epsilon}_{33} \\ \dot{\epsilon}_{12} \end{pmatrix} = \underline{\mathcal{C}}(\underline{\sigma}) \begin{pmatrix} \dot{\sigma}_{11} \\ \dot{\sigma}_{22} \\ \dot{\sigma}_{33} \\ \dot{\sigma}_{12} \end{pmatrix} \tag{12}$$

with $\underline{\mathcal{C}}(\underline{\sigma})$

$$= \begin{pmatrix} a + \frac{h(\kappa)}{4\mu\kappa^2}s_{11}^2 & b + \frac{h(\kappa)}{4\mu\kappa^2}s_{11}s_{22} & b + \frac{h(\kappa)}{4\mu\kappa^2}s_{11}s_{33} & \frac{h(\kappa)}{2\mu\kappa^2}s_{11}\sigma_{12} \\ b + \frac{h(\kappa)}{4\mu\kappa^2}s_{22}s_{11} & a + \frac{h(\kappa)}{4\mu\kappa^2}s_{22}^2 & b + \frac{h(\kappa)}{4\mu\kappa^2}s_{22}s_{33} & \frac{h(\kappa)}{2\mu\kappa^2}s_{22}\sigma_{12} \\ b + \frac{h(\kappa)}{4\mu\kappa^2}s_{33}s_{11} & b + \frac{h(\kappa)}{4\mu\kappa^2}s_{33}s_{22} & a + \frac{h(\kappa)}{4\mu\kappa^2}s_{33}^2 & \frac{h(\kappa)}{2\mu\kappa^2}s_{33}\sigma_{12} \\ \frac{h(\kappa)}{4\mu\kappa^2}s_{11}\sigma_{12} & \frac{h(\kappa)}{4\mu\kappa^2}s_{22}\sigma_{12} & \frac{h(\kappa)}{4\mu\kappa^2}s_{33}\sigma_{12} & \frac{1}{2\mu} + \frac{h(\kappa)}{2\mu\kappa^2}\sigma_{12}^2 \end{pmatrix} \tag{13}$$

---

[1] With the : denoting the appropriate tensor product.

$$\kappa^2 = \frac{1}{2} s_{ij} s_{ij} = \frac{1}{3} \left[(\sigma_{11} - \sigma_{33})^2 + (\sigma_{22} - \sigma_{33})^2 \right.$$
$$\left. - (\sigma_{11} - \sigma_{33})(\sigma_{22} - \sigma_{33}) \right] + \sigma_{12}^2$$
$$a = \frac{1}{9K} + \frac{1}{3\mu}$$
$$b = \frac{1}{9K} - \frac{1}{6\mu}$$
$$h(\kappa) = \frac{\mu}{\mu_p(\kappa)} - 1 \tag{14}$$

with the Bulk modulus $K = \frac{E}{3(1-2\nu)}$.

We will use the following definitions for plane strain:

$$V = (\nu_1, \nu_2, \epsilon_{11}, \epsilon_{22}, \epsilon_{33}, \epsilon_{12})^T \tag{15}$$

$$U = (\nu_1, \nu_2, \sigma_{11}, \sigma_{22}, \sigma_{33}, \sigma_{12})^T \tag{16}$$

with which the 2-D system can be written in the general form (6), (7) again.

The most important difference between the elastic wave equation and the standard wave equation $\phi_{tt} - c^2 \Delta \phi = 0$ is the existence of several wave modes. In the elastic case there are compression waves (P-waves) with wave-speed $c_1 = \sqrt{\frac{K+4/3\mu}{\rho}}$ and shear waves (S-waves) with wave-speed $c_2 = \sqrt{\frac{\mu}{\rho}} < c_1$. In plastic regions we find an additional fast plastic wave c_f and a slow plastic wave c_s with $c_s < c_2 < c_f < c_1$ (cf. [9–17]).

3
The numerical approach

The most appropriate approach (cf [4]) is to solve the two parts of the system (6), (7) separately in each time step (i.e. solving the flux (6) with a PDE-solver and the ODE (7) with an ODE-solver), instead of trying to re-arrange them to a closed-form PDE. The reason for this ansatz are numerical problems, e.g. the right-hand side of the ODE (7) can be discontinuous (depending on the hysteresis model). We discuss these two steps in the following, since they will be the basis for the simulation of crack problems. For solving the PDE we use the method of transport, for solving the ODE-part of the system we apply a high-order Runge-Kutta solver.

The approach presented ensures high-order simulations for both – the PDE part and the stress-strain relationship, which results in a computational advantage compared to other methods, (e.g. [9–14]) using a first-order reconstruction of the stress-strain relationship only.

3.1
The method of transport

The basic idea of the method of transport is to rewrite the flux Eq. (6) equivalently as a coupled system of advection equations. Therefore, we introduce a set of direction vectors $\vec{n}_i$, $i = 1, \dots, k$, not necessarily of unit length, which have to fulfill the following two consistency relations:

$$\sum_{i=1}^{k} \vec{n}_i = 0, \quad \frac{1}{k} \sum_{i=1}^{k} \vec{n}_i \vec{n}_i^T = \underline{I} \tag{17}$$

With these definitions we can rewrite the flux Eq. (6) (or 11) as follows:

$$V_t + \nabla \cdot c\underline{L} = 0 \tag{18}$$

$$\Longleftrightarrow \frac{1}{k} \sum_{i=1}^{k} \{ (V + \underline{L}\vec{n}_i)_t + \nabla \cdot c(V + \underline{L}\vec{n}_i)\vec{n}_i^T \} = 0 \tag{19}$$

$$\Longleftrightarrow \sum_{i=1}^{k} \{ (R_i)_t + \nabla \cdot c\, R_i \vec{n}_i^T \} = 0$$

with the identity matrix $\underline{I}$ and the quantities $R_i = \frac{1}{k}(V + \underline{L}\vec{n}_i)$. We observe that our flux equation can be written as a system of coupled advection equations, each of which transports the quantity R_i at the velocity $c\vec{n}_i$.

Note that Eq. (19) is strictly equivalent to the original Eq. (18). Our approximation consists of decoupling the system, i.e. at a certain time-step t^n we define the independent quantities

$$R_i(\vec{x}, t^n) := \frac{1}{k}(V(\vec{x}, t^n) + \underline{L}(\vec{x}, t^n)\vec{n}_i) \tag{20}$$

and then solve the advection equations

$$(R_i)_t + \nabla \cdot (R_i c\vec{n}_i^T) = 0 \quad \forall i \tag{21}$$

independently, i.e. we calculate the quantities $R_i(\vec{x}, t)$ on the time interval $t \in [t^n, t^{n+1}]$ using Eq. (21) and given the initial solution $R_i(\vec{x}, t^n)$. At the next time-step t^{n+1} the update for the vector V reads:

$$V(\vec{x}, t^{n+1}) = \sum_{i=1}^{k} R_i(\vec{x}, t^{n+1}) \tag{22}$$

This yields a first order approximation for the exact solution in time if the consistency relations (17) hold, since then

$$V_t = \sum_{i=1}^{k} (R_i)_t = -\sum_{i=1}^{k} \nabla \cdot (cR_i \vec{n}_i^T) = -\nabla \cdot c\underline{L}.$$

and consequently

$$V(\vec{x}, t^n + \Delta t) - \sum_{i=1}^{k} R_i(\vec{x}, t^n + \Delta t) = \mathcal{O}(\Delta t^2)$$

However, to obtain approximations of higher order in time one has to add correction terms into the numerical fluxes, i.e. one uses slightly modified quantities in the advection equations

$$R_i := \frac{1}{k}(V + (\underline{L} + \underline{K})\vec{n}_i)$$

where the correction matrix $\underline{K}$ can be found by comparing the Taylor expansion of the exact solution to the expansion of the numerical scheme, which we show for the 2-D case (i.e. $\vec{x} = (x, y)^T$) in the following (the 3-D case is analogous). The derivation of the correction terms is quite similar to the derivation of the second order Lax-Wendroff scheme (cf. [16]).

For the exact solution of Eq. (6) we obtain:

$$V(\vec{x}, t_0 + \Delta t) = V(\vec{x}, t_0) + \Delta t V_t(\vec{x}, t_0) + \frac{\Delta t^2}{2} V_{tt}(\vec{x}, t_0) + \dots$$

The flux Eq. (6) in 2-D can be rewritten in the form (since it is linear)

$$V_t = \underline{A} U_x + \underline{B} U_y$$

with two constant matrices $\underline{A}$ and $\underline{B}$. Taking into account the definition of V and U (Eqs. (15) and (16)) and the stress-strain relationship (12) it is straightforward to see that a linear relationship of the form

$$U_t = \underline{\mathcal{A}}(\underline{\sigma}) V_t \tag{23}$$

exists with a matrix $\underline{\mathcal{A}}$.

Now, we can easily replace derivatives in time by spatial derivatives:

$$V_t = \underline{A} U_x + \underline{B} U_y = \nabla \cdot [\underline{A} U, \underline{B} U] \tag{24}$$

$$V_{tt} = \underline{A}(U_t)_x + \underline{B}(U_t)_y$$

$$= \nabla \cdot \{[\underline{A}, \underline{B}](\underline{\mathcal{A}}(\underline{\sigma}) V_t)\} \tag{25}$$

$$=: \nabla \cdot \underline{Z} \tag{26}$$

The Taylor expansion of the advection Eq. (21) is:

$$R_i(\vec{x}, t_0 + \Delta t) = R_i(\vec{x}, t_0) + \Delta t (R_i)_t(\vec{x}, t_0)$$

$$+ \frac{\Delta t^2}{2}(R_i)_{tt}(\vec{x}, t_0) + \ldots \tag{27}$$

Using the advection equation (21), time derivatives can be replaced by spatial derivatives:

$$(R_i)_t = -\nabla \cdot (R_i \vec{n}_i^T c) \tag{28}$$

$$(R_i)_{tt} = -\nabla \cdot ((R_i)_t \vec{n}_i^T c) = \nabla \cdot ((\nabla \cdot (R_i \vec{n}_i^T c)) \vec{n}_i^T c)$$

Obviously, our scheme is first order accurate since

$$\sum_{i=1}^{k} R_i(\vec{x}, t_0) = V(\vec{x}, t_0)$$

$$\sum_{i=1}^{k} R_i(\vec{x}, t_0) \vec{n}_i^T c = c\underline{L}$$

which gives

$$\sum_{i=1}^{k} (R_i)_t(\vec{x}, t_0) = V_t(\vec{x}, t_0) = -\nabla \cdot c\underline{L}(\vec{x}, t_0)$$

$$= -\sum_{i=1}^{k} \nabla \cdot (R_i(\vec{x}, t_0) \vec{n}_i^T c) \tag{29}$$

However, comparing Eq. (24) to (28) it turns out that the second order derivatives in time are not the same:

$$V_{tt} - \sum_{i=1}^{k} (R_i)_{tt} = \nabla \cdot \left(\underline{Z} + \sum_{i=1}^{k} (R_i)_t \vec{n}_i^T c \right) = \nabla \cdot \underline{\bar{K}} \neq 0 \tag{30}$$

with $\underline{\bar{K}} := \underline{Z} + \sum_{i=1}^{k} (R_i)_t \vec{n}_i^T c$. We define the correction matrix $\underline{K}$ by

$$\underline{K} = \frac{\Delta t}{2} \underline{\bar{K}} \tag{31}$$

and the transported quantities $\tilde{R}_i$ by

$$\tilde{R}_i := \frac{1}{k} \left(V + (\underline{L} + \frac{1}{c}\underline{K})\vec{n}_i \right) \tag{32}$$

Equation (29) still holds for the $\tilde{R}_i$ ($\Longrightarrow$ the scheme is still consistent). Furthermore, one can easily verify:

$$\sum_{i=1}^{k} (\tilde{R}_i)_t(\vec{x}, t_0) = \sum_{i=1}^{k} (R_i)_t(\vec{x}, t_0) - \frac{\Delta t}{2} \nabla \cdot \underline{\bar{K}} \tag{33}$$

and consequently

$$V(\vec{x}, t_0 + \Delta t) - \sum_{i=1}^{k} \tilde{R}_i(\vec{x}, t_0 + \Delta t) = \mathcal{O}(\Delta t^3)$$

Our decomposition is now of second order, since the second order error (30) is compensated by the correction term appearing in the first order derivative of $\tilde{R}_i$. Third and fourth order can be achieved analogously.

The integration of the decoupled advection Eqs. (21) can be written in a simple explicit form, since the wave-speed c is constant:

$$R_i(\vec{y}, t) = \int_{IR^2} R_i(\vec{x}, t^n) \delta(\vec{y} - [\vec{x} + c\vec{n}_i \Delta t]) d\vec{x} \tag{34}$$

Moreover, there is an infinite number of possible propagation vectors that fulfill the consistency relation (17), e.g. one could simply use the four diagonal directions $\vec{n}_i = (\pm 1, \pm 1)^T$. However, to obtain better numerical results (e.g. results closer to the analytic solution if available) it is advantageous to chose a "wave-model" $\vec{n}_i$ that takes into account the physical behavior of the system, e.g. the decomposition into advection equations based on the wave-model $\vec{n}_i$ should reduce to the 1-D decomposition into right eigenvectors if one simulates a 1-D problem. A very advanced wave-model fulfilling this physical requirement was presented in [5], which we will use for the numerical calculations in this paper. The scheme will be consistent if and only if the consistency relation (17) holds, independent of the wave-speed c that appears in the flux (6) and the decomposition (19). For stability reasons the wave-speed c used for solving the advection equations has to be set to the highest physical propagation speed that can appear, i.e. c_1 – as shown by ([2, 3]), this requirement is equivalent to fulfilling the traditional CFL-condition.

So far our discussion has been semi-discrete only, since we haven't discretized the space variables yet. The space discretization can be done as for all types of finite volume methods, i.e. one has to add the following two steps:

• At a certain time-level one computes cell-averages for each cell I_{ij} (we assumed a grid in 2-D) for the quantity V according to Eq. (22):

$$\bar{V}_{ij}^{n+1} = \frac{1}{|I_{ij}|} \sum_{l=1}^{k} \int_{I_{ij}} R_l(\vec{y}, t^{n+1}) d\vec{y} \tag{35}$$

• Before each time-step one has to reconstruct the function $V(\vec{x}, t)$ by polynomials in space from the previously updated cell-averages.

3.2
Stress update
The method of transport discussed above only yields an update of V, i.e. the velocity and strain variables. The stress variables $\underline{\sigma}$ have to be updated by integrating the

ODE (12) in time. The problem is that the strain variables $\underline{\boldsymbol{\epsilon}}$ are only known at the discrete time-levels t^n and t^{n+1}. However, to integrate Eq. (12) in time we have to know the derivative $\underline{\boldsymbol{\epsilon}}_t$ on the whole time-interval $[t^n, t^{n+1}]$. Therefore, we reconstruct the strain-path in time by polynomials in time:

$$\underline{\boldsymbol{\epsilon}}(\vec{x}, t) = \underline{\boldsymbol{\epsilon}}(\vec{x}, t^n) + \underline{\boldsymbol{a}}(\vec{x})(t - t^n) + \underline{\boldsymbol{b}}(\vec{x})(t - t^n)^2$$
$$+ \ldots \quad \forall t \in [t^n, t^{n+1}] \tag{35}$$

Since we can compute the time derivatives of the strain variables at time t^n and t^{n+1} by using

$$\frac{\partial}{\partial t} \epsilon_{ij}(t^*) = \frac{1}{2}\left(\frac{\partial v_j}{\partial x_i} + \frac{\partial v_i}{\partial x_j}\right) \tag{36}$$

$$\frac{\partial^2}{\partial t^2} \epsilon_{ij}(t^n) = \frac{1}{2\rho} \sum_k \left(\frac{\partial^2}{\partial x_i \partial x_k} \sigma_{ik} + \frac{\partial^2}{\partial x_j \partial x_k} \sigma_{jk}\right)(t^n)$$
$$at \quad t^* = t^n \quad or \quad t^{n+1} \tag{37}$$

(v_i is known at time t^n and t^{n+1} after the PDE-time-step and σ_{ij} is known at time t^n) we can reconstruct the behavior of the strain variables in time. Further, with the help of this reconstruction one can integrate the stress-strain relationship (12). It is important to note that during the integration a transition from elasticity to plasticity might occur where the right hand side of the ODE is discontinuous. In such a case one has to find the exact transition point (e.g. by bisection or with Newton's method) and then restart the ODE-solver at this point (cf. Fig. 2).

Although we will demonstrate the accuracy of our method by simulations on a Cartesian grid only, it is important to mention that the same approach (consisting of solving advection equations for the PDE and solving an ODE for th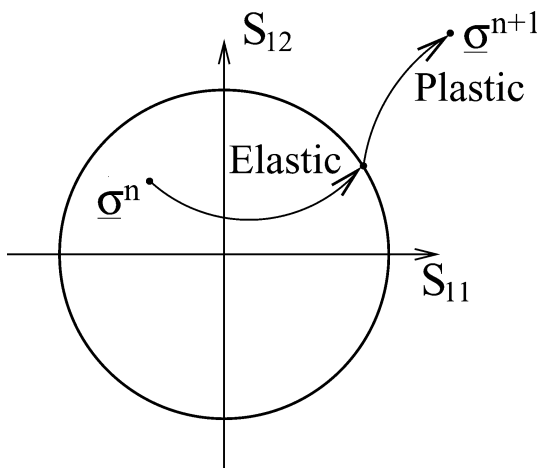e stress-strain relationship) can be used on irregular grids as well – the only extra effort consists of implementing a solver for advection equations on a non-Cartesian grid.

4
Crack problems for plane-strain

For our numerical examples, we consider a cracked plate in 2-D under plane-strain as shown in Fig. 3. The crack is modelled by assuming that along both sides of the crack there is a free boundary up to the crack-tip. In contrast to numerical methods that are based on an adjusted numerical grid around the crack (especially at the crack-tip), we simulate the dynamical behavior of elastic-plastic waves hitting the crack on a standard Cartesian grid but using numerical approximations of high (i.e. up to fourth) order, which is advantageous from an implementation point of view as well as for ensuring a fast computation of numerical results.

In the following numerical simulation, we assume that from both sides of the crack a compression wave is approaching, as indicated in Fig. 3.

Since the crack is assumed to be a free boundary within the solid, we have to impose the following boundary conditions along both sides of the crack:

$$\sigma_{22} = \sigma_{12} = 0$$

Which basically means that the normal force along the free boundary vanishes.

For all computations a grid of 500×500 cells is used for the entire simulation and the results are plotted after 240 time-steps (which corresponds to $t = 0.96$) for all simulations – we only plot the solutions at one point in time, since they look self-similar in time. The crack faces are assumed to be traction free and crack face contact is excluded in the simulation. Further, for all computations we plot the maximal shear stress around the crack-tip, since this variable typically illustrates the physical phenomena very well and makes our results comparable to other authors (e.g. [9–14]).
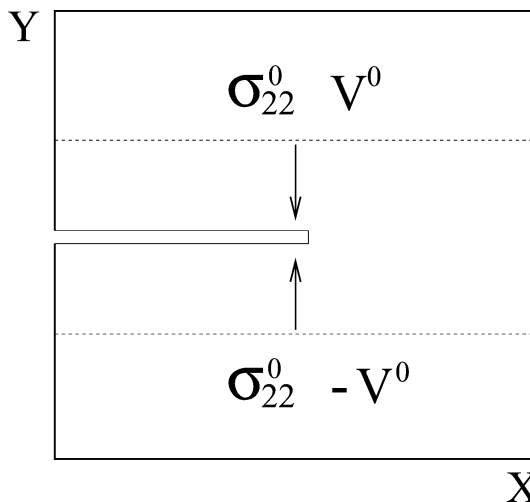
Fig. 2. Integration of the stress-strain relationship in the stress space from $\underline{\boldsymbol{\sigma}}^n$ to the new state $\underline{\boldsymbol{\sigma}}^{n+1}$ The ODE-solver has to be restarted on the yield surface (i.e. the level set of the yield function in the stress space separating elastic from plastic states) since the ODE can be discontinuous at the transition from elasticity to plasticity

Fig. 3. Compression waves carrying the velocity $\pm v_2^0$ and the stress component σ_{22}^0 approaching a crack
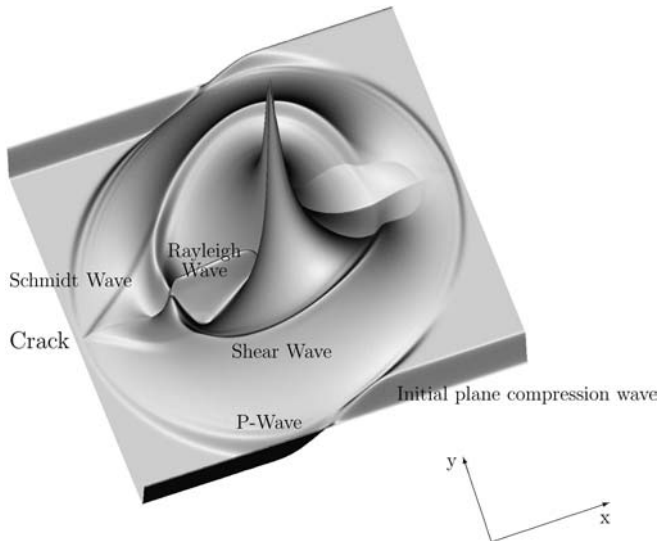
Fig. 4. Numerical computation of the maximal shear stress around the crack-tip in the elastic case. The singularity, the compression wave, the shear wave, the Rayleigh wave and the von Schmidt wave are well resolved (grid: 500×500 cells)

Fig. 5. Computation of the maximal shear stress around the crack-tip for an elastic-plastic material. Due to the very high stress intensity at the crack-tip, a zone of plastic deformation occurs at the crack-tip, which is indicated by the level-sets of the yield-variable κ in the area of $\kappa > 1$ (grid: 500×500 cells)

Figure 4 shows a computation of the maximal shear stress for a purely elastic material with

$$c_1 = \sqrt{\frac{K + \frac{4}{3}\mu}{\rho}} = 1 \quad c_2 = \sqrt{\frac{\mu}{\rho}} = \frac{1}{\sqrt{3}}$$

The initial conditions for the compression waves are chosen as

$$v_2^0 = 0.55 \quad \sigma_{22}^0 = \frac{v_2^0}{c_1} \quad \sigma_{11}^0 = \sigma_{33}^0 = \frac{v_2^0(K - 2/3\mu)}{c_1} \quad \sigma_{12}^0 = v_1^0 = 0$$

In the following Fig. 4 we plot the maximal shear stress for the computed approximation.

Obviously, all physical aspects are well resolved: a circular compression wave travelling at c_1 and a circular shear wave travelling at c_2 are created at the crack-tip. At the free boundary of the crack, a Rayleigh wave is travelling along the surface of the crack at a speed less than c_2. Further, the circular P-wave propagating along the free surface of the crack produces a von Schmidt travelling at speed c_2, which has the shape of a cone since $c_2 < c_1$. Moreover, at the crack-tip the stress becomes singular.

The problem becomes even more interesting if we allow plastic deformation. We choose the same initial conditions for the compression waves and the initial value for the yield parameter is chosen as

$$\kappa_0 = 1.$$

We further assume $\mu_p(\kappa) \equiv const$ with

$$\frac{\mu_p}{\mu} = \frac{3}{16}$$

In addition to the physical behavior observed for the elastic solid, a zone of plastic deformation is created at the crack-tip, as can be seen from Fig. 5, where the intensity of the stress becomes so large that the yield criterion is fulfilled and the material is in the state of plastic flow.
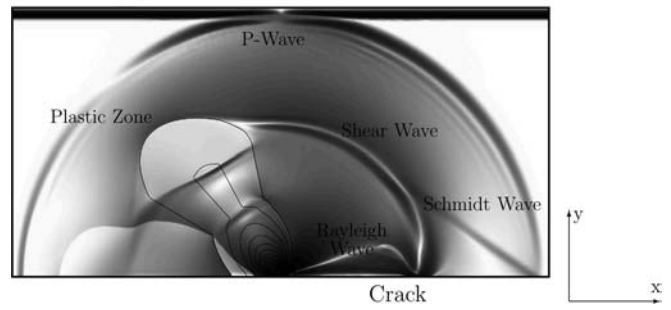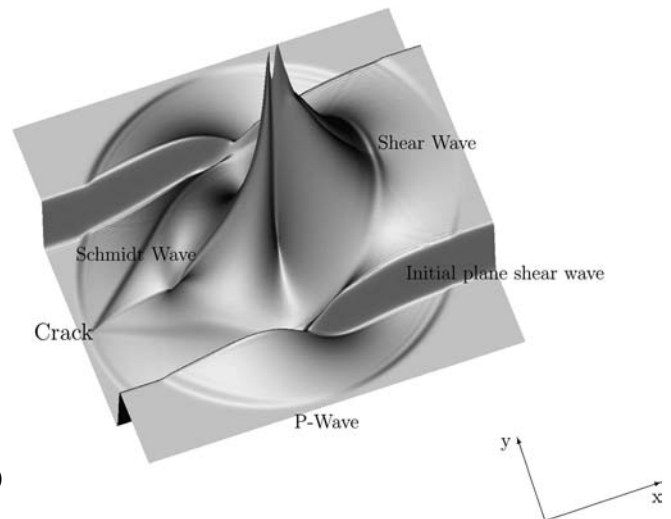

Fig. 6. Maximal shear stress in the cracked plate for an elastic material. The wave phenomena are similar to those in Figure (4) (grid: 500×500 cells)

We now consider the same crack but this time shear waves are approaching from both sides of the crack. The initial conditions are chosen as

$$v_1^0 = 0.55 \tag{38}$$

$$\sigma_{12}^0 = \frac{\mu}{c_2} v_1^0$$

$$\sigma_{11}^0 = \sigma_{22}^0 = \sigma_{33}^0 = v_2^0 = 0 \tag{39}$$

Figure 6 shows the elastic and Fig. 7 the plastic case.

As for compression waves hitting a crack, various wave phenomena are created at the crack-tip, i.e. a circular compression and a shear wave. Furthermore, a von Schmidt wave is created at the free boundary of the crack. In addition to this, the second example shows a plastic zone, again indicated by the contour lines for the yield-variable $\kappa > 1$. Since the slow plastic wave speed c_s is constant with

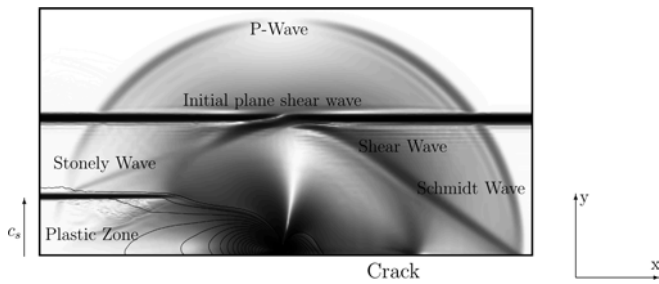$$\frac{c_p}{c} = \sqrt{\frac{\mu_p}{\mu}} = \sqrt{\frac{3}{16}}$$

Fig. 7. Maximal shear stress in the cracked plate including plastic deformation (grid: 500 × 500 cells)

we observe a plane c_s-wave propagating behind the discontinuous shear wave. Since the wave-speeds in the plastic and elastic region are different ($c_2 > c_s$), a conic head wave is produced by the P-wave travelling along the border between elasticity and plasticity, analogous to the von Schmidt wave at a free boundary.

The numerical computations show that the structure of the physical wave phenomena including plastic flow around the crack is well resolved in all examples, although they were computed on the simplest grid possible, i.e. a Cartesian grid, which is due to the use of approximations of high order in space and time.

5
Conclusion

Although the elastic-plastic wave equation is not a pure conservation law known from fluid-dynamics, we could use the Method of Transport combined with a high-order Runge-Kutta ODE-solver to simulate plastic waves in solids in high order. The method we presented can be used up to any order in space (by reconstructing the solution by polynomials after each time-step) and in time (by using correction terms in the numerical flux) and it can be used with any kind of hysteresis model, which can be described by an ODE at every point. Furthermore, Fey showed in [2, 3] that the Method of Transport can be used for nonlinear conservation laws, which shows that our method is not limited to the linearized model of small strains. Compared to other methods (cf. introduction) the Method of Transport has the advantage that it can be implemented to any order in space and time and hence it allows high resolution simulations with less computation time.

Further, we showed by numerical examples that the use of high-order schemes for elastic-plastic waves is especially advantageous when simulating cracks in solids, since the singularities in the stress and the complex structure of waves created at the crack-tip require a very high resolution of the physical behavior of solids, in particular when using a Cartesian grid without grid-refinement near the

crack(-tip). Using a Cartesian grid is advantageous from both an implementation and a computation effort point of view, but only reasonable when using a numerical scheme of very high order in space and time.

References

1. **Colella P** (1990) Multidimensional upwind methods for hyperbolic conservation laws. SIAM J. Comput. Phys. 87: 171–200
2. **Fey M** (1998) Multidimensional Upwinding. Part I. The method of transport for solving the euler equations. J. Comput. Phys. 143: 159–180
3. **Fey M** (1998) Multidimensional upwinding. Part II: decomposition of the euler equations into advection equations. J. Comput. Phys. 143: 181–199
4. **Giese G, Fey M** (2003) High order simulation of the elastic-plastic wave equation in two space dimensions". Wave Motion, 38(4): 327–343
5. **Giese G, Fey M** (2002) A genuinely multi-dimensional high-resolution scheme for the elastic-plastic wave equation. J. Comput Phys 181: 338–353
6. **Gould PL** (1983) Introduction to linear elasticity. Springer, Berline Heidelberg New York
7. **Kröner D** (1997) Numerical schemes for conservation laws. Wiley Teubner
8. **LeVeque RJ** (1992) Numerical methods for conservation laws. Lectures in mathematics. Birkhäuser
9. **Lin X** (1996) Numerical computation of stress waves in solids. Akademie Verlag
10. **Lin X, Ballmann J** (1995) Improved bicharacteristic schemes for two-dimensional elastodynamic equations. Quart. Appl. Math LIII 2: 383–398
11. **Lin X, Ballmann J** (1995) A numerical scheme for axisymmetric elastic waves in solids. Wave Motion 21: 115–126
12. **Lin X, Ballmann J** (1995) Numerical modelling of elastic-plastic waves in transversely isotropic composite materials. ZAMM 75: 267–268
13. **Lin X, Ballmann J** (1995) Elastic-plastic waves in cracked solids under plane stress. In: Wegner JL, Norwood FR (eds) Nonlinear waves in solids. ASME book No. AMR 137, pp. 155–160
14. **Lin X, Ballmann J** (1994) Numerical modelling of elastic-plastic deformation at crack tips in composite material under stress wave loading. J. Phys. III C8-53-58
15. **Lubliner J** (1990) Plasticity theory. Macmillan Publishing Company, cop.
16. **Morton KW, Richtmyer RD** (1995) Difference methods for initial-value problems. Krieger Publishing Company
17. **Nowacki WK** (1978) Stress waves in non-elastic solids. Oxford, Pergamon Press
18. **Prandtl L** (1924) Proceedings of the first international congress for applied mechanics. Delft, p. 43
19. **Roe P** (1981) Approximate riemann solvers, parameter vectors and difference schemes. J. Comput. Phys., 43: 357–372
20. **Serre D** (1999) Systems of conservation laws. Cambridge University Press
21. **Ning Nan TC, Ting T** (1969) Plane wave due to combined compressive and shear stresses in half space, J. Appl. Mech.